



Visualization of shallow subseafloor fluid migration in a shallow gas hydrate field using high-resolution acoustic mapping and ground-truthing and their implications on the formation process: a case study of the Sakata Knoll on the eastern margin of the Sea of Japan

Miho Asada¹ · Mikio Satoh¹ · Manabu Tanahashi¹ · Toshiyuki Yokota¹ · Shusaku Goto¹

Received: 28 December 2021 / Accepted: 1 August 2022 / Published online: 22 August 2022
© The Author(s) 2022

Abstract

Acoustic mapping enables an understanding of the surface distribution of shallow gas hydrate (GH) and related products. Acoustically characteristic materials such as fluid-seepage-related methane-derived authigenic carbonate and/or shallow GHs, may be widely distributed beneath the shallow seafloor of the Sakata Knoll. High-amplitude reflectors over the knoll are the top of gas-bearing permeable layers and connect to the reverse fault at the foot of the knoll. Shallow GH and bacterial mats were observed at the high-amplitude layer cut by depression and/or the locally disturbed seafloor. Acoustic blanking zones observed on the sub-bottom profiler sections are current gas migration routes from the depth to the seafloor. Optical observations indicate that fluid seepage is not active in the current seafloor, and it is not necessarily observed above the acoustic blanking zones or shallow faults reaching the seafloor. In the Sakata Knoll, the tectonically formed reverse fault and gas-bearing permeable layers play more important roles in fluid migration from depth to the summit area of the knoll compared to acoustic blanking and shallow faults. The depression at the summit area of the Sakata Knoll was formed by the dissociation of a shallow GH at around the last glacial maximum. Limited fluid seepage is currently witnessed within and around the depression and it is less extensive than that in the past. Such knolls, with tectonically formed large faults and an anticline are abundant in the area and they can be good reservoirs for shallow GH along the eastern margin of the Sea of Japan.

Keywords Shallow gas hydrate · Acoustic mapping · Acoustic blanking · Subseafloor distribution · Sakata Knoll

Introduction

Natural gas hydrates (GHs) and related features on the seafloor, even if covered with thin sediments, are typically observed via acoustic mapping. Acoustic mapping can facilitate an understanding of the features, for instance, the extent and distribution of bathymetric features such as various sized pockmarks and mounds and shallow subseafloor structures (e.g., Judd and Hovland 2007). Acoustic mapping also

helps identify materials with a characteristic distribution of backscatter strengths, provided that the physical properties of the material differ from those of neighboring ones. These features might indicate the presence and status of natural GHs on the seafloor and the shallow subseafloor.

GH is a kind of clathrate in which water molecules form a cage around a single molecule of natural gas; this material is widespread in permafrost regions and beneath the ocean floor (Kvenvolden 1988; Ginsburg 1998) as GH is stable under low temperature and high-pressure conditions (Sloan 1998; Ruppel and Kessler 2017). GH at a shallow depth of ~ 100 m below the seafloor is called “shallow GH” (Expedition 311 Scientists 2006). In many cases, methane is the primary component of natural gas; hence, natural GH is often referred to as methane hydrate. The methane released from GH might have caused the stepwise global warming of

✉ Miho Asada
asada.miho@aist.go.jp

¹ Research Institute for Geo-Resources and Environment, Geological Survey of Japan, National Institute of Advanced Industrial Science and Technology (AIST), Tsukuba Central 7, 1-1-1 Higashi, Tsukuba, Ibaraki 305-8567, Japan

the Paleocene as discussed in previous studies (e.g., Dickens et al. 1995; Matsumoto 1995; Bains et al. 1999; Ruppel and Kessler 2017); hence, the distribution and characteristics of GH have been extensively investigated (e.g., Sloan 1998; Ruppel and Kessler 2017).

The occurrence of a shallow GH has been investigated along the eastern margin of the Sea of Japan in areas with a water depth of 500–1000 m to elucidate shallow GH occurrences (Matsumoto 2009; Matsumoto et al. 2011). Along this, multiple datasets (e.g., using research vessels, autonomous underwater vehicles (AUVs), remotely operated vehicles (ROVs), and sediment coring and logging while drilling (LWD) operations) have been acquired over the last decade in these areas. Here, we report the results of recent acoustic observations by a research vessel and an AUV, as well as ground-truthing data via an ROV, to show the present status of shallow GH, related features, and the past activities of the summit area of a spindle-shaped knoll, on a km-scale positive topographic feature in the northeast part of the Sea of Japan (hereafter referred to as Sakata Knoll).

Geological background

The Sea of Japan is a back-arc basin between the eastern margin of the Eurasian continent and the Japan arc. It is believed to have formed approximately 24–15 million years ago (Ma) (e.g., Otofujii et al. 1985; Tamaki 1988; Okamura et al. 1995; Nakajima 2018); however, the exact age and details remain debated. During the following period, the Sea of Japan closed from the surrounding ocean and underwent anoxic conditions during 12–10 Ma and petroleum source rocks were deposited during this period (Nakajima 2018). Approximately 6 Ma and later, the Sea of Japan was laid under the northwest to the southeast compressional stress field. Some of the existing normal faults that formed during the rifting stage have been reactivated as thrusts. Topographic features characteristic of tectonic inversion, reactivated faults, and the formation of anticlines have occurred from 6 Ma to the present (Tamaki 1988; Okamura et al. 1995; Nakajima 2018).

The Mogami Trough is ~250 km long at ~50 km off the coast of northeast Japan with water depths ranging from 500 to 3000 m (Nakajima et al. 1996) (Fig. 1). A series of reverse faults along the Mogami Trough were activated by tectonic inversion from the Miocene to the present (Okamura et al. 1995; Matsumoto et al. 2009). Fine-grained clay-dominant sediments cover most of the Mogami Trough (Watanabe 1992; Ikehara et al. 1994; Nakajima et al. 1996). A small amount of sandy sediment was found in the turbidites (Ikehara et al. 1994).

The Sakata Knoll is a spindle-shaped or elongated domal knoll, with a summit water depth of ~530 m located in the

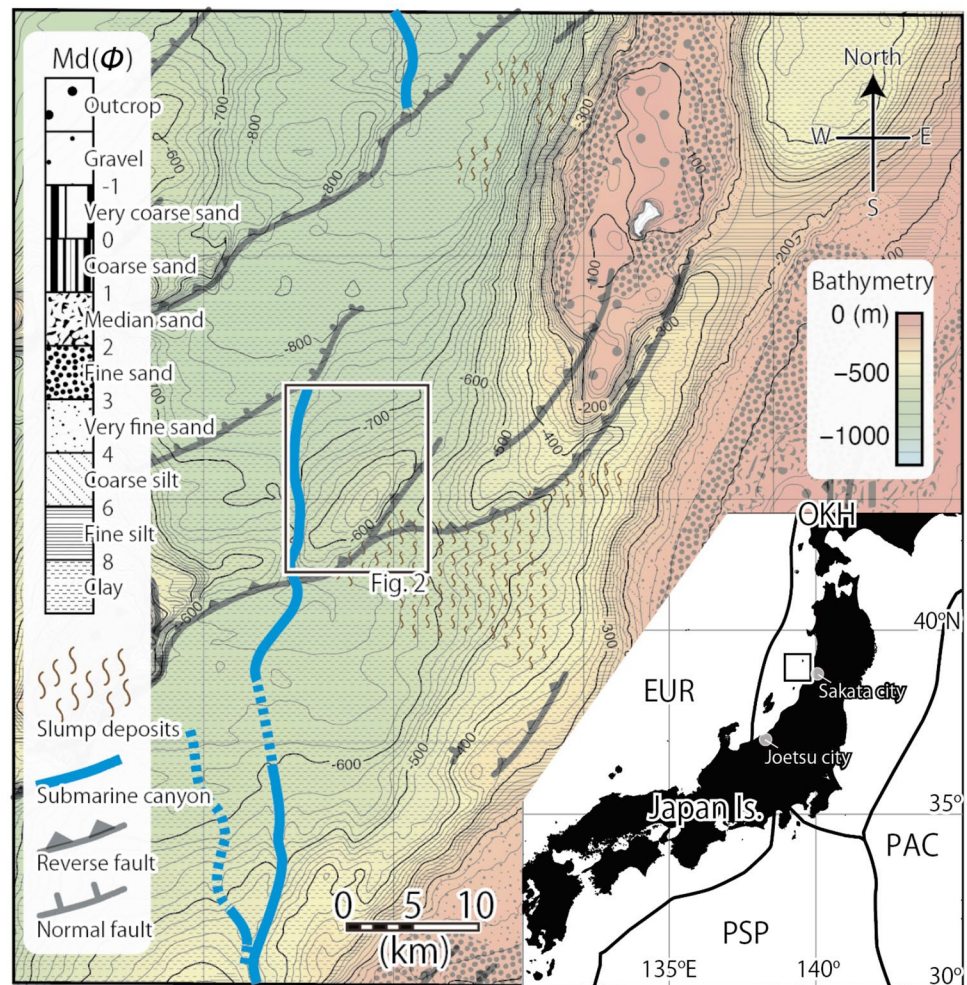
Mogami Trough (Fig. 2). Several massive GHs were sampled by sediment coring from 8 to 21 m below the seafloor (Miyajima et al. 2022), and wider distribution of the GH was strongly indicated by three-point LWD measurements (Tanahashi et al. 2017) at the summit area of the knoll. The size of the Sakata Knoll is ~15 km along the major axis and 5–10 km along the minor axis, with a relative height of ~120 m to the surrounding flat seafloor. The slope is asymmetric about the major axis, steep to the southeast, and relatively gentle to the northwest. The Sakata Knoll is bounded by the Mogami deep-sea channel to the west and a minor channel to the east. The knoll is characterized by a ramp anticline with the reverse fault at the southeastern foot, which thrusts up from northwest to southeast (Okamura et al. 1995). Buried slump deposits have been identified below a flat seafloor on the southeastern side of the knoll (Ikehara et al. 1994; Okamura et al. 1996). The surface sedimentation rate is estimated to be ~30 cm-per-thousand years (cm/kyr), based on the occurrence of *Pseudoenotia doliolus* (diatom fossils) in a ~450 cm-long gravity core sample from the slump deposits, and it is 10.2 cm/kyr based on the tephrochronology of a ~290 cm-long piston core sample at the northwestern slope of the knoll (Watanabe 1992; Ikehara et al. 1994) (Fig. 2a).

Data acquisition

Acoustic mapping using a Research Vessel Kaiyomaru No.1 (Kaiyo Engineering Co., Ltd., Japan) in 2020 (Fig. 2) and an AUV Deep1 (Fukada Salvage & Marine Works Co., Ltd., Japan) in 2014 (Fig. 3) was conducted over the Sakata Knoll. Subseafloor profiles were also obtained along the same survey lines with the acoustic mapping (Figs. 4 and 5). Ground-truthing for acoustic mapping was obtained using the ROV Kaiyo3000 (Kaiyo Engineering Co., Ltd., Japan) at the summit area of the knoll in 2020 (Fig. 6).

AUV Deep1 surveyed the summit area of the Sakata Knoll with three pieces of acoustic equipment: multibeam echo sounder (MBES; Socnic2022, R2Sonic, USA), side-scan sonar (2200 M, EdgeTech, USA), and sub-bottom profiler (SBP; 2200 M, EdgeTech, USA). The frequencies of MBES, side-scan sonar, and SBP were 200 kHz, 118.75–131.25 kHz, and 2–8 kHz, respectively. During our investigations, the AUV maintained a cruising height of ~50 m above the seafloor and a cruising speed of ~3 knots (~5.5 km/h). The AUV mapping covered an approximate area of 4.9 km × 2.2 km, with 30 lines across the crest and one tie line along the crest of the knoll (Fig. 3). The final output of bathymetry data was a 3-m gridded image. Side-scan sonar data were processed by SonarWiz (Chesapeake Technology Inc., CA, USA) and it produced an output of a 3-m gridded backscatter image. SBP data have also been

Fig. 1 Bathymetric map including survey area. Patterns on the map indicate the distribution of sediment types classified by particle size (Md , Ikehara et al. 1994) and geological information (Okamura et al. 1996). The rectangle shows the shipboard acoustic observation area (Fig. 2). Blue line: submarine canyon. Gray line: fault. *PSP* Philippine Sea Plate; *PAC* Pacific Plate; *OKH* Okhotsk Plate; *EUR* Eurasia Plate. Background color and contour indicates bathymetry quoted from Kisimoto (2000)



imaged via SonarWiz. The SBP sections show subseafloor images of ~50 m below the seafloor with a vertical resolution of ~0.2 m (Fig. 4).

Acoustic mapping, using hull-mounted equipment (MBES and SBP) onboard the Research Vessel Kaiyomaru No.1, was conducted over the Sakata Knoll, including the area of AUV observation. The frequency and ship speed for MBES (EM122, KONGSBERG, Norway) were 12 kHz and ~7 knots (~13 km/h), respectively. MBES data were processed by HIPS and SIPS version 5 (Teledyne CARIS, Canada). The resulting bathymetry and backscatter strength distribution images were output at 15-m and 4-m resolutions, respectively (Fig. 2). Shipboard SBP data (SBP-120, KONGSBERG, Norway) were obtained at a chirp frequency of 2.5–7 kHz (Fig. 5) and showed subseafloor images of ~50 m below the seafloor with a vertical resolution of ~0.2 m.

Seafloor images for ground-truthing were obtained using an ROV Kaiyo3000 and ROV HAKUYO3000 (Fukada Salvage & Marine Works Co., Ltd., Japan) at the summit area of the Sakata Knoll (Fig. 6). A

three-dimensional pictorial mapping system, SeaXerocks1 (Bodenmann et al. 2016), is a fixed payload of the ROV Kaiyo3000. It took ~16 pictures every second and provided a detailed relief of the seafloor surface with a laser beam from 4 to 5 m altitude at a cruising speed of 0.2–0.4 knot. Relief data and optical images were then combined to create 3D point cloud data. The nominal resolutions of the resulting 3D image across and along the track were ~2 mm (equal to the number of pixels in images) and ~30 cm (depending on cruising speed), respectively. The observed results provide optical images with less distortion because the images have been taken from directly above the seafloor. The image provided quantitative optical information on the seafloor environment, such as the distribution and size of biological communities and outcrops on the seafloor (Fig. 6).

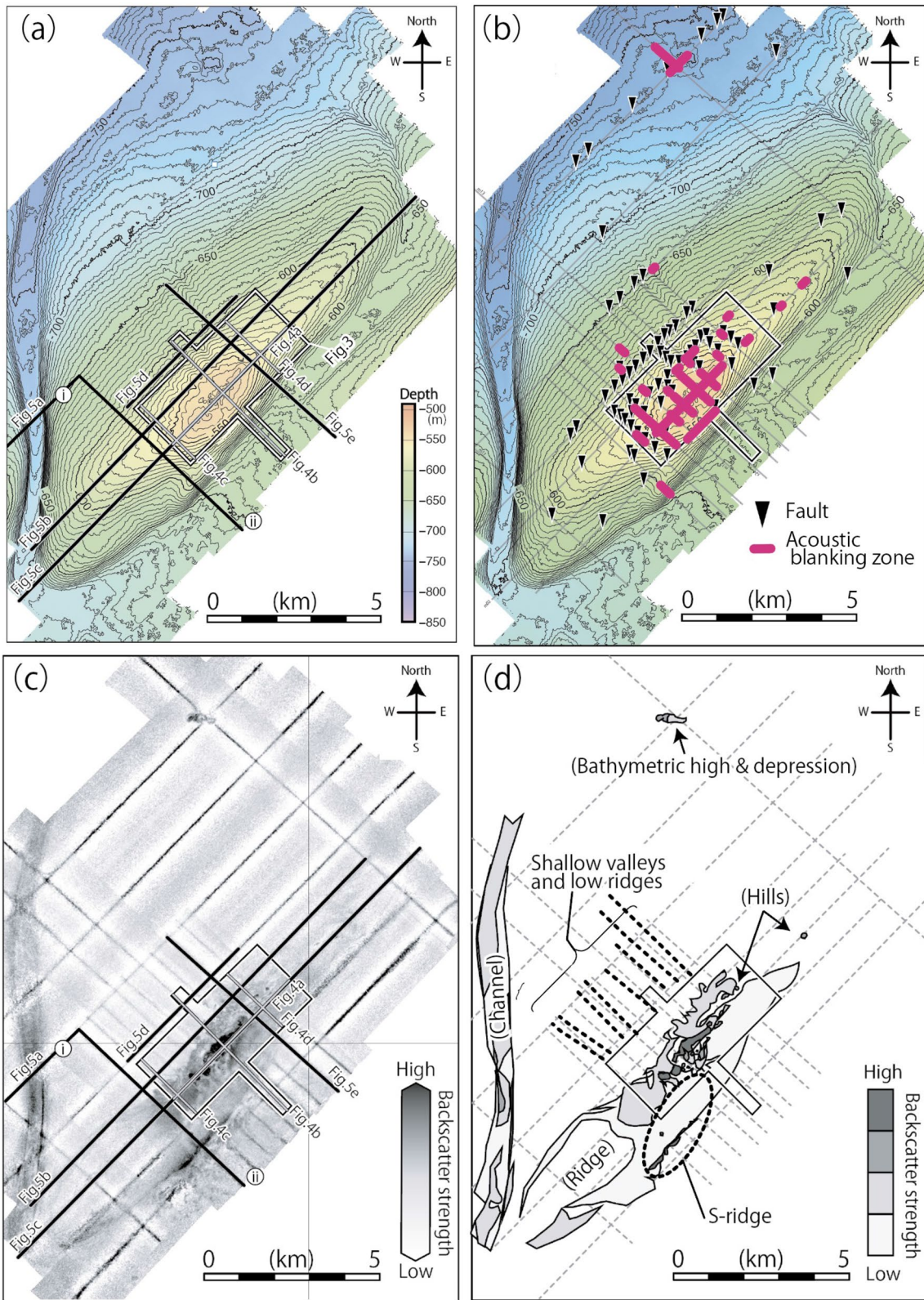


Fig. 2 Shipboard acoustic observation results. The location of the observations is indicated by the black rectangle in Fig. 1. Polygon on the map: AUV observed area (Fig. 3). **a** Bathymetry of study area obtained by 1K20 cruise in 2020. The contour interval is 5 m. White bold line: location of AUV-mounted sub-bottom profiler (SBP) section (Fig. 4). Black bold line: shipboard SBP survey line (Fig. 5). Circled numbers (i and ii): sediment core sampling points measuring sedimentation rate, (i) 10.2 cm/kyr and (ii) 27.5 cm/kyr (Ikehara et al. 1994). **b** Distribution of faults (triangles) and acoustic blanking zones (purple lines) indicated by shipboard SBP sections. Thin gray line: shipboard survey lines. **c** Backscatter strength distribution, darker color indicates higher backscatter strength. White and black bold lines, circled numbers coincide with (a). **d** Interpretation of backscatter strength distribution

Results

Acoustic mapping and ground-truthing of seafloor

A depression and surrounding features at the summit area of the knoll, based on AUV and ROV observations

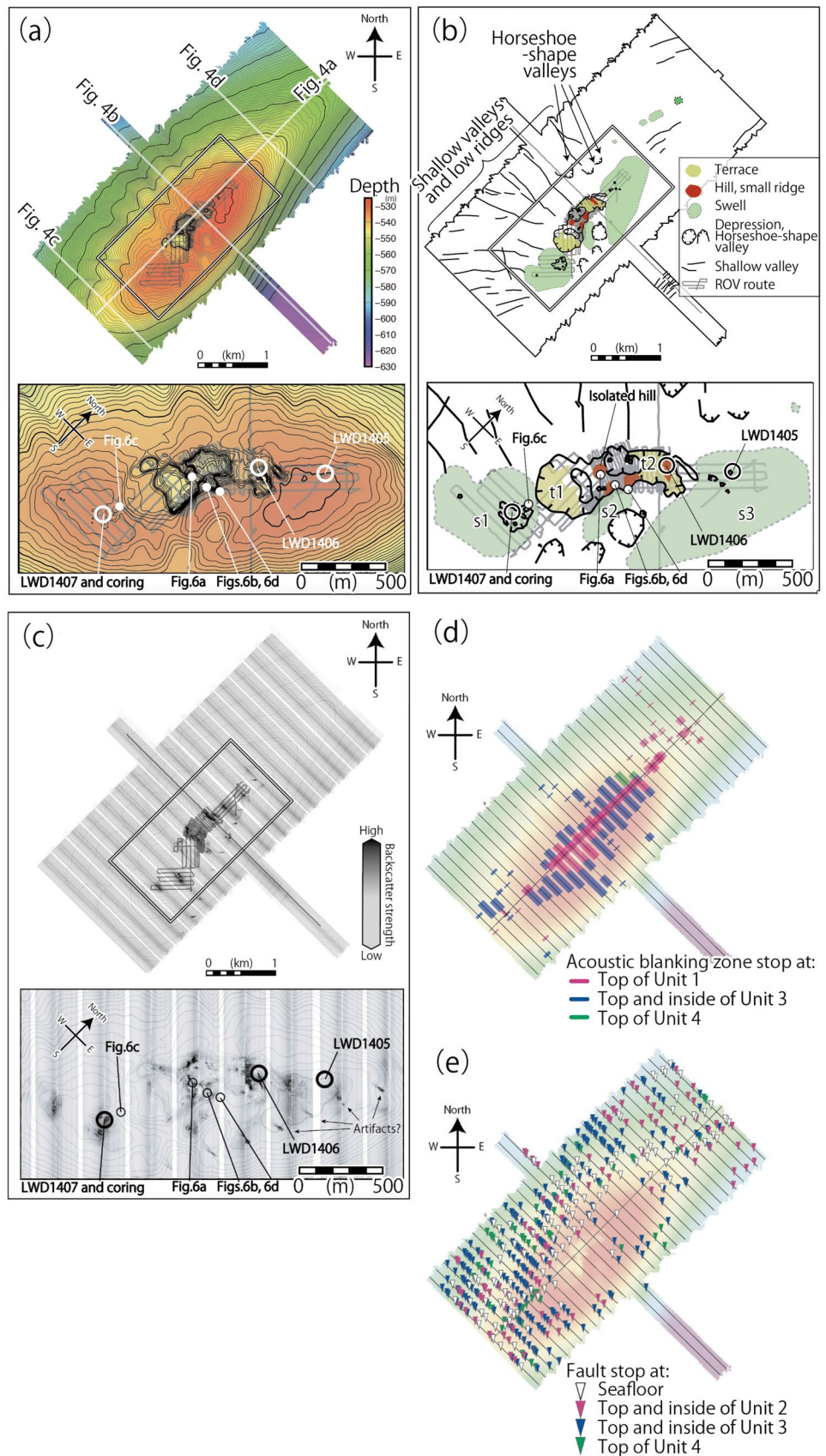
The target knoll is an asymmetric anticline with a NE-SW axis with a steep SE side (hereafter, we refer to the slope as SE-slope) and a gentle NW side (NW-slope). High-resolution bathymetry data displayed a depression at the summit area of the knoll that extended approximately along the direction of the major axis (Fig. 3a). The size of the depression was ~ 1000 m along the axis, 300–400 m across the axis, and the maximum depth and length around the deepest part of the depression were ~ 12 m and ~ 500 m along the axis, respectively. The outer rims of the deepest part are bordered by two inner terraces on the northeastern and southwestern sides and scarps occur on the NW-slope and SE-slope sides (Fig. 3a). There are bathymetric highs in the center of the depression, an isolated hill with a height of ~ 12 m on the NW-slope side and small ridges on the SE-slope side (Fig. 3b). The backscatter strength distribution over the depression was generally low in flat areas, and patchwork-like highs and lows were observed around the isolated hill, small ridges, and on the inner scarp on the SE-slope side within the depression (Fig. 3c). Optical observation via ROV revealed many small-scale bacterial mats and outcrops (Fig. 6, see Fig. 3a for positions) over the small ridges and an isolated hill, which are consistent with the areas of patchwork-like high-backscatter distribution. In particular, dense and linear bacterial mats were observed underneath a similarly linear outcrop almost along isobaths on the inner scarp on the SE-slope side (Fig. 6b). The bottom of the deepest part of the depression tended to be covered with sediments and had no bacterial mats and outcrops, which are consistent with a low-backscatter distribution. Throughout the entire area of ROV observation, outcrops appeared as an assemblage of dark- to light-gray-colored and irregularly shaped blocks of a few to several dozen cm in size. The outcrops

are considered carbonate rocks that are commonly reported on the seafloor in methane seepage areas (Matsumoto et al. 2009; Numanami and Matsumoto 2009). We found no GH exposure on the seafloor via ROV observations and no bubbling indications via acoustic and ROV observations. Bathymetric features suggesting collapse and/or mass movement connecting to the depression were not observed.

Two terraces at the southwestern and northeastern inner ends of the depression were located at a depth of ~ 5 m from the edge of the depression but they appeared to be very different from each other. The southern terrace (“t1” in Fig. 3b, bottom) showed a half-circle and a relatively flat seafloor. The low-backscatter strength indicated that the terrace was thickly covered by sediments. The ROV observation was consistent with the sedimented seafloor devoid of outcrops and bacterial mats. The northern terrace (“t2” in Fig. 3b, bottom) differed from the southern terrace in terms of acoustic characteristics having a complex shape, being surrounded by steep slopes, and with a higher backscatter strength than that of t1, especially on the inner ridge. The ROV observation showed several outcrops and bacterial mats on t2, consistent with the rough seafloor and a relatively high-backscatter distribution on t2. One of three-point LWD measurements (LWD1406, M04L) was conducted on the t2 and it strongly suggested the presence of GH between just below the seafloor to a depth of ~ 30 m, based on sonic velocity log, gamma-ray, and resistivity data (Tanahashi et al., 2017).

At least three swells (bathymetric inflations: “s1”–“s3” in Fig. 3b, bottom) were identified outside the depression via AUV observation. The swell s1 was located on the southwestern extension of the crest from the depression and it was ~ 4 m higher than the depression boundary. There was a partially caved seafloor at the top, north (depression-side) of s1, with a locally high-backscatter strength. The ROV observation showed local outcrops and bacterial mats on the rough seafloor and the northern side, and the rest of the areas on s1 were covered by sediments. Several massive GHs have been sampled from 8 to 21 m below the seafloor by sediment coring from the s1 (Miyajima et al. 2022). The LWD1407 (M05L) measurement was also conducted on the s1, and they suggest the presence of GH below the seafloor (Tanahashi et al. 2017). The swell s2 was located on the eastern side of the depression, which is ~ 4 m above the boundary of the depression, with a relatively flat seafloor and high-backscatter strength. The swell s3 is located on the northeastern extension of the crest and it is approximately 2 m high relative to the depression. Swell s3 is larger and flatter than the other swells. The backscatter strength was slightly higher on the west side of s3 (depression-side) and it gradually decreased toward the northeast. ROV observations showed patches of bacterial mats and outcrops on sediment in an area with a higher backscatter strength. The last LWD1405 (M03L) measurement conducted on the s3 also

Fig. 3 Acoustic observation results obtained by AUV. The target area is indicated by the polygon in Fig. 2. Point of LWD measurements and photo images (Fig. 6) indicated by the circle in the bottom, which displays a magnified image from the box on the map. **a** Bathymetry map. The contour interval is 0.5 m. White line: locations of AUV-based SBP sections (Fig. 4). Gay line: track line of ROV observations. **b** Interpretation of (a) showing bathymetric features; t1: southern terrace, t2: northern terrace, s1: southern swell, s2: swell located on the eastern side of the depression, and s3: northern swell. **c** Backscatter strength distribution, darker color indicates a higher backscatter strength. **d** Distribution of acoustic blanking zones indicated by SBP sections obtained by AUV. Colored bar: depth of top of acoustic blanking zones. **e** Distribution of faults indicated by SBP sections obtained by AUV. Colored triangle: depth of top of faults



suggested the presence of GH below the seafloor (Tanahashi et al. 2017).

Shipboard acoustic observations revealed a different pattern of backscatter strength distribution compared to AUV observations

Shipboard acoustic observations showed a similar pattern to AUV observations for bathymetric features at the summit area of the knoll but a different pattern for backscatter strength distribution. Over the depression and swells, the shipboard backscatter strength pattern was uniformly high (Fig. 2d), while AUV showed variously high and low-backscatter strength patterns (Fig. 3c). At the same time, a significantly wider range of high-backscatter strength than the AUV observations were shown by the ship from the summit area to surrounding areas in all directions. In particular, a complex high- and low-backscatter strength distribution was observed on the NW-slope near the crest (Fig. 2c, d). A part of the relatively high-backscatter area extended toward ridge branches from the southwestern extension of the crest to the south (hereafter referred to as S-ridge). A spot of high-backscatter strength was identified on the S-ridge (Fig. 2c, d), indicating that it preserves similar acoustic characteristics as that of the summit area of the knoll. Bathymetric features suggesting collapse and/or mass movement connecting to the depression were not observed over the wider area as well.

Descriptions of other features observed by AUV and vessels

Radially distributed low ridges and shallow valleys are bathymetric features that were recognized over the southern part of the NW-slope near an outer margin of the area observed by AUV (Fig. 3a, b) and were continuous north-westward as shown by shipboard acoustic observation (Fig. 2d). Backscatter strengths over the ridges and valleys were generally low, indicating that these ridges and valleys are mostly covered by sediments (Fig. 3b). Other shallow and horseshoe-shaped valleys were clearly shown on the southern part of the SE-slope and central part of the NW-slope by AUV observation (Fig. 3c). Backscatter strength was low in these valleys, implying that the seafloor was also covered by sediment. Such negative topographic features are more common over the relatively southern part of the knoll. Conversely, positive topographic features except for three swells, such as small hills, were more common on the northern part of the knoll (Fig. 3b). The shipboard observations revealed spots of high-backscatter strength overlapping with small hills, whereas AUV observation revealed low-backscatter strength in the same region (Figs. 2d and 3c). Few spots of high-backscatter strength indicated by the shipboard observation (Fig. 2c) were also identified at the S-ridge and the northeastern extension of the crest of the

knoll, corresponding to the location of other small hills. These subseafloor structures are described in the following SBP section. Another geological feature, a pair of a mound and a depression, was observed in the northern part of the area observed by the shipboard, showing high-backscatter strength on the mound (Fig. 2).

Shallow structures below the seafloor

SBP sections were acquired both by the AUV and the vessel with the acoustic mapping surveys. Both AUV-equipped and shipboard SBPs use a similar frequency, with a similar penetration of ~50 m and a similar vertical resolution of ~0.2 m. The AUV-equipped SBP has a shorter distance to the target, making it possible to shorten the interval of transmitting acoustic signals and narrow apertures, such that it has a higher lateral resolution. The SBP sections showed stratigraphy that was roughly consistent with the topography depicting a large anticline. The sections display some high-amplitude layers and an “acoustic blanking” zone, which is a mostly a vertical zone with almost no reflection signal, shown on SBP sections and distributed below the depression and other areas. We have converted the vertical axis of the SBP sections from two-way travel time to depth, assuming a uniform acoustic velocity of 1500 m/s (Figs. 4 and 5).

AUV-based SBP sections

Based on the subsurface acoustic stratigraphy shown by SBP records, we identified four stratigraphic units and three notable reflectors. The reflectors change their amplitude along the horizons, and sometimes the high-amplitude part shifts to adjacent layers (Fig. 4).

Unit 1 is the uppermost unit between the seafloor and Reflector-I, which disappears in the depression and on swells; thus, Reflector-I appears at the seafloor in the depression and on swells. Unit 2 is a section between Reflectors I and II, showing little change in thickness, which slightly reduces and is dragged upward toward the depression edge. Unit 3 significantly decreases in thickness as it approaches the depression and exhibits the greatest thickness variation among the four units, divided into two subunits by Reflector-III: Unit 3a (upper part) and 3b (lower part). Unit 3a has a characteristic transparent zone that lies between Reflectors II and III, while Unit 3b is an alternating layer of relatively transparent and reflective zones laying below Reflector-II. The SBP profile shows that the lower limit of Unit 3b is an unconformity, and it is not always evident. Unit 4 includes parallel, stratified, and continuous thin layers over the profiles. The lower limit of Unit 4 sometimes exceeds the limit of detection of SBP sections, and hence, Unit 4 was set as the lowermost unit in our SBP sections description. The

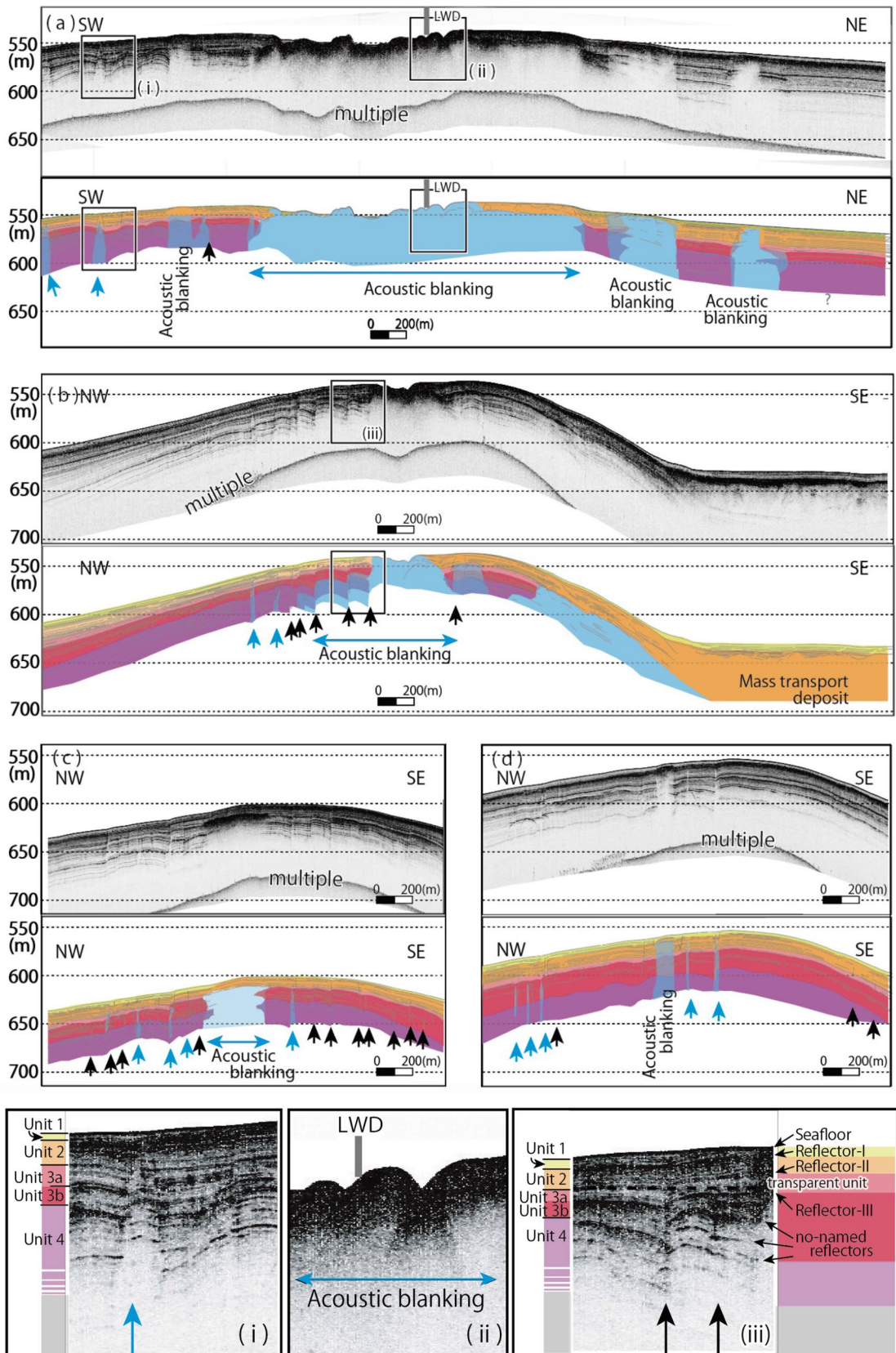


Fig. 4 a–d: SBP sections obtained by AUV and their interpretations. Double blue arrow: range of acoustic blanking. One-way blue arrow: fault with acoustic blanking. One-way black arrow: fault without acoustic blanking zone. Position of LWD1406 measurement (in the northern terrace, t2 in Fig. 3b) located in the SBP section (Tanahashi et al. 2017) is indicated by bold gray line in (a). (i)–(iii) Magnified images coincide with boxes (i)–(iii) in Fig. 4a–d. (i) Fault with acoustic blanking zone, which stops at the top of Unit 2. (ii) A part of the acoustic blanking zone. (iii) Fault without acoustic blanking zone, which stops at the top of Unit 3

penetration of SBP's signals was generally small on the SE-slope. The details of each unit are as follows:

Unit 1 becomes thicker and more pronounced toward the foot of the knoll and toward the northern part of the knoll. Unit 1 over the SE-slope, especially in the southern part of the slope, is seemingly hidden by the thickened Reflector-I. Unit 1 becomes thinner and finally disappears as it approaches the depression. Sometimes patchy transparent sediment on Reflector-I is identified inside the depression, but those sediments are not connected to Unit 1 in the SBP sections. Unit 1 tends to be thin on the southern part of the SE-slope (Fig. 7). Unit 1, covering the southeastern foot of the knoll, where a reverse fault is suggested, is continuous toward the flat southern area.

Unit 2 appears at the bottom of the depression of the knoll crest, where Unit 1 loses its lateral continuity (Fig. 4). Thickness variance shows that Unit 2 tends to be thinnest on the southern part of the NW-slope, which is the opposite side of the thinnest part of Unit 1 (Fig. 7). Unit 2 includes a chaotic pattern under the southeastern foot of the knoll, across which a reverse fault is suggested, which is interpreted as a mass transport deposit confirmed by seismic reflections over the area (Ikehara et al. 1994; Okamura et al. 1996). Because Unit 2 is continuous over the knoll and does not show a large collapse connecting to the mass transport deposit at the southeastern foot of the knoll, the deposit is considered of external origin.

Unit 3 has a high-amplitude Reflector-II at the top, Reflector-III between subunits 3a and 3b, and contains other high-amplitude reflectors within the unit. Unit 3a, an upper subunit of Unit 3, has a characteristic transparent zone containing intermittently obscured layers. Unit 3a was clearly visible in the southern part of the knoll but it was difficult to identify in the northern part of the knoll. Unit 3a touches the top of some acoustic blanking zones, while Unit 3b, lying underneath Unit 3a, contacts the side of the acoustic blanking zones. Unit 3b includes fine layers and changes its form to wedge-shaped, thinning toward acoustic blanking. Unit 3b contains relatively transparent zones, especially on the SE-slope side of the knoll. There are significant anticlines cut by multiple faults in the area below the low ridges and shallow valleys at the southern part of the NW-slope. The lowermost part of Unit 3b is an obscure layer and it is an unconformity.

Changes in thickness and deformation were observed to be smaller in the northern part of the knoll (see Fig. 7).

Unit 4 was the lowermost unit that could be recognized in SBP sections, and it is cut by the same multiple faults as that of Unit 3b. Unit 4 is deformed along with Unit 3, yet it appears to maintain a constant thickness even if cut. Several unnamed high-amplitude reflectors were also observed within Unit 4.

The “acoustic blanking” zone is an acoustic expression that masks most of the structures on SBP sections (Fig. 4). Obscure layers could be observed inside the acoustic blanking zone in some cases. The acoustic blanking zones are divided into two types: (1) broadly distributed and masking most subseafloor structures (see Fig. 4a, b), and (2) very thin features that also mask structures and are sometimes accompanied by faults (see Fig. 4c, d). Acoustic blanking zones widely appear over the summit area of the knoll in several separated sections (Fig. 3d). The outstanding broad one was located below the depression and neighboring area, extending ~3 km along the crest (Fig. 4a). Others were identified in several parts relatively distant from the outstanding one. Most of the acoustic blanking zones in the southern part of the knoll had high-amplitude caps and relatively broad widths and tended to stop at the top of Unit 3a. On the contrary, acoustic blanking zones in the northern part of the NW-slope were very thin and vertical, tending to stop at the top of Unit 2, and sometimes accompanying a diffraction wave when the acoustic blanking zone crossed reflectors in Unit 4 (Fig. 4d). None of the acoustic blanking zones penetrated Unit 1 to the seafloor.

Normal faults are dominant within the SBP sections when they have adequate displacements. We refer to the faults as “shallow faults” to distinguish them from the tectonically formed reverse fault on the southeastern foot of the knoll. Some shallow faults accompany acoustic blanking zones, while others do not (Fig. 4). Despite the difficulty in identifying the distribution of shallow faults because of the acoustic blanking zones masking the subseafloor features, the density of the shallow fault seemed to be high on the NW-slope and southern part of the knoll but smaller on the SE-slope and northern part of the knoll (Fig. 3e). Most of the shallow faults that cut Units 3 and 4 seemed to stop at the top of and within Unit 3. Shallow faults that cut Unit 1 (reaching the seafloor) formed ~23% of the total and were mostly located on the NW-slope.

Shipboard SBP sections

SBP data obtained by surface vessels had a lower resolution than those obtained by AUV; however, we could follow the distribution of Unit 1 over a wider area than the area observed by AUV. Unit 1 is continuous between two regions [regions (i) and (ii) in Figs. 2a and 5c], whose sedimentation

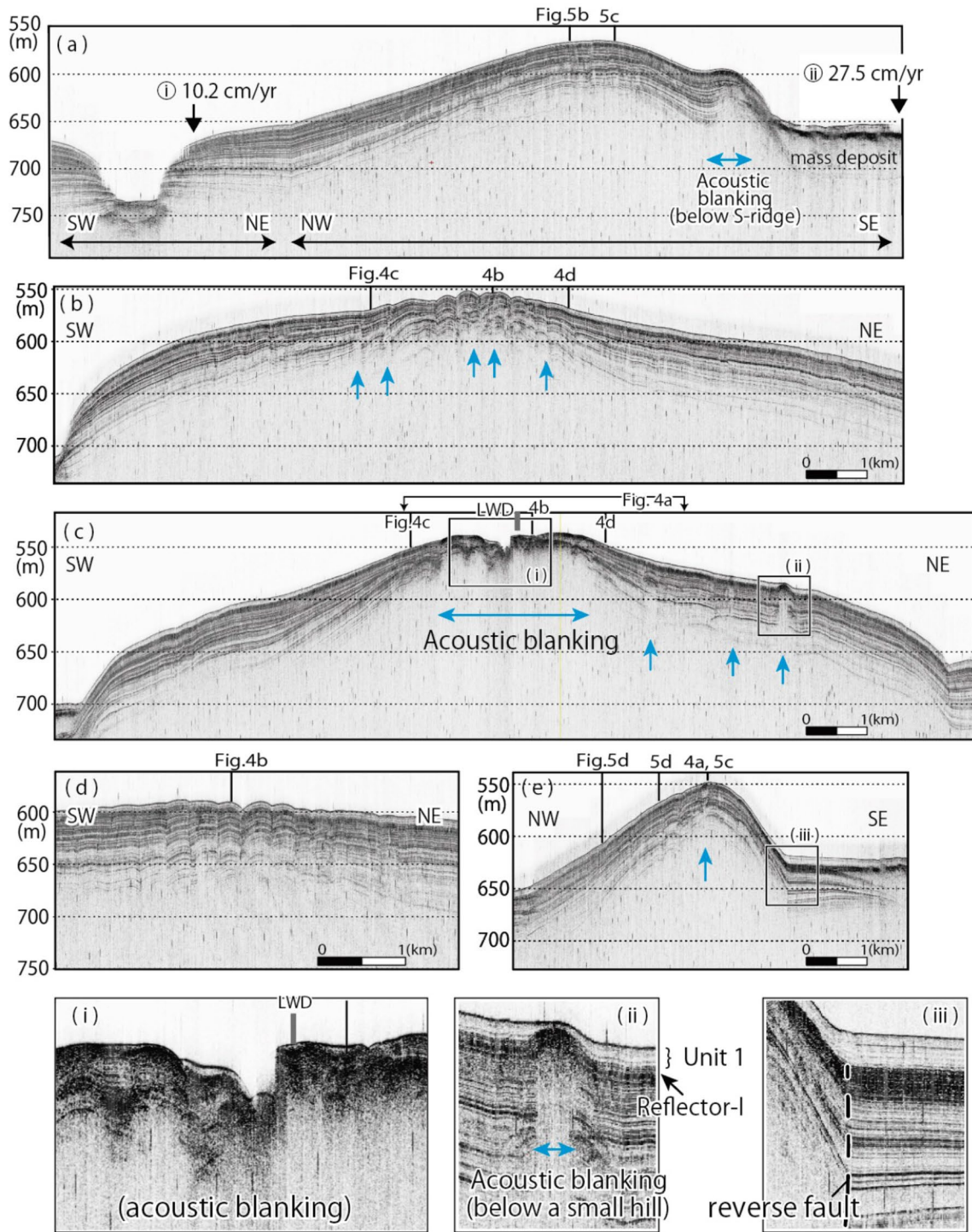


Fig. 5 a–e: Shipboard SBP sections, magnified images coincide with boxes (i)–(iii). Double blue arrow: range of acoustic blanking zone. One-way blue arrow: acoustic blanking zone. Bold gray line: position of LWD measurement in SBP section (Tanahashi et al. 2017). Sediment core sampling points are indicated in (a). (i) Acoustic blanking

zone covered by thin sediment layer (Unit 1). (ii) Acoustic blanking zone below a small hill which is not penetrating Unit 1. (iii) Fault at the southeastern foot of the Sakata Knoll interpreted as a tectonically formed reverse fault (dotted line)

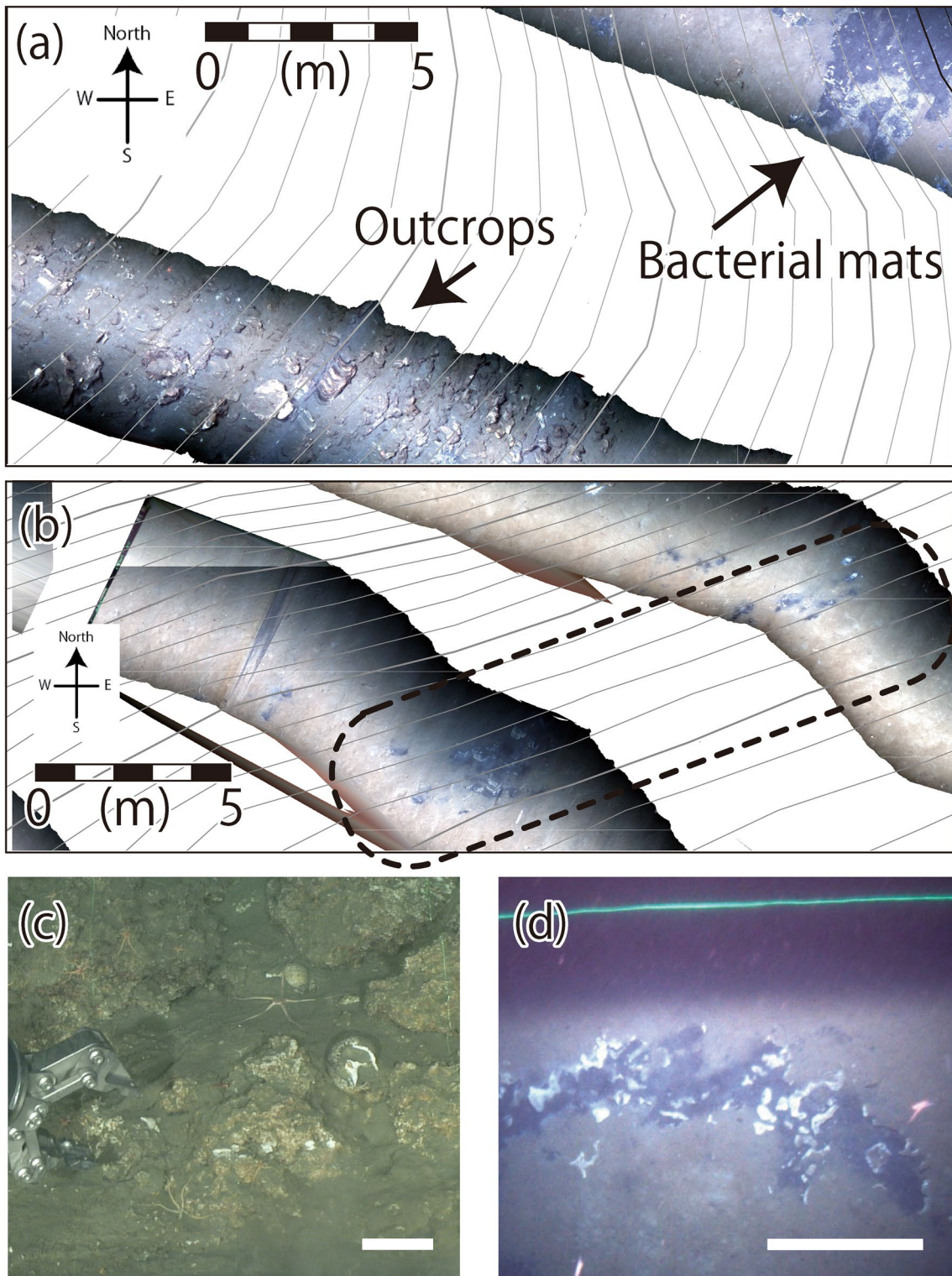


Fig. 6 Images obtained by ROVs. See Fig. 3, magnified bottom image, for exact position of (a)–(d). **a** Mosaic image by SeaXerocks1 displays closely distributed black colored bacterial mat and outcrops. Gray lines indicate 0.2 m intervals of contour line obtained by acoustic observation using AUV. **b** Mosaic image by SeaXerocks1 displays white- and black-colored bacterial mats that appear roughly aligned with the isobath of the local scarp, indicated by gray con-

tour lines (0.2-m intervals). **c** Photo image of outcrop taken by ROV HAKUYO3000. White line indicates approximately a 0.1-m scale. **d** Photo image of bacterial mat lies under outcrops, taken by ROV-Kaiyo3000 and SeaXerocks1. Green line in the image is the laser beam measured relief data. White line indicates approximately a 1-m scale

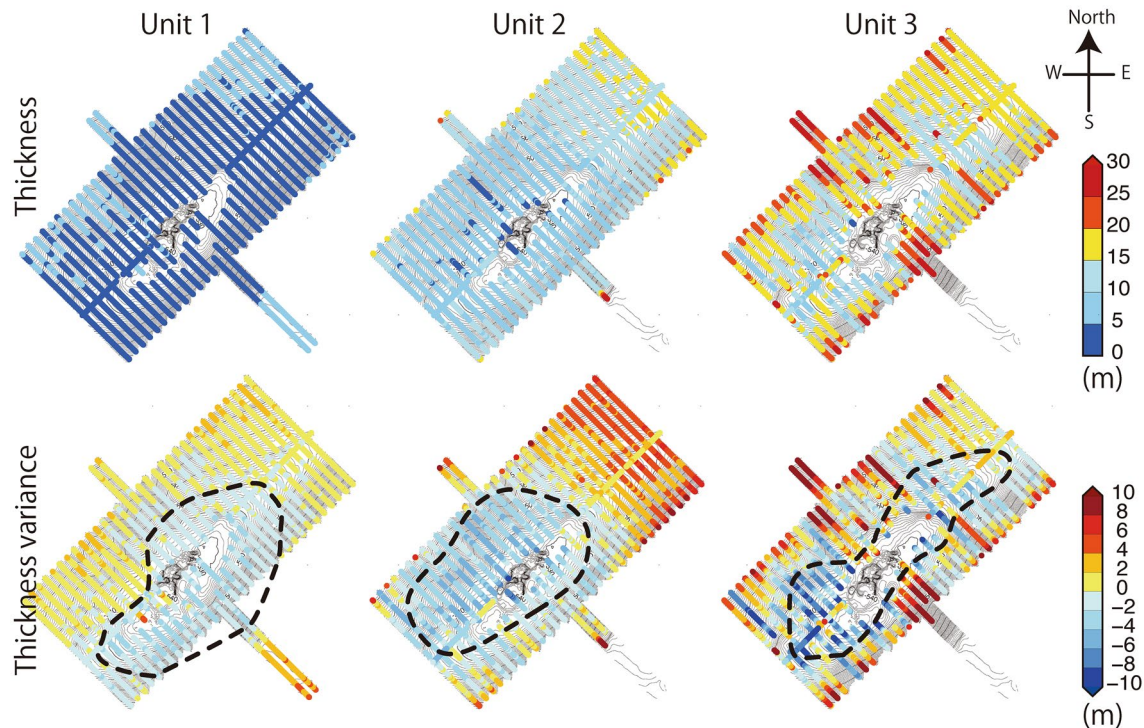


Fig. 7 Thickness (upper) and thickness variance of Units 1–3 (lower). The thickness variance shows the result of subtracting the thickness of each point from the average thickness of each unit. A dotted circle

indicates the location of the thin part of each unit. Note that the thin part (area circled by dotted line) has moved

rate was estimated from surface sediments (Ikehara et al. 1994), to calculate the approximate formation period of Unit 1. The region with a 10.2 cm/kyr sedimentation rate (Ikehara et al. 1994), region (i), is located in the western part of the knoll close to the Mogami deep-sea channel. The thickness of Unit 1 in the region (i) is 3–4 m, which implies that the age at the bottom of Unit 1 is approximately 29–32 kyr. In another region on the southeastern side of the knoll, region (ii), with a sedimentation rate of 27.5 cm/kyr (Ikehara et al. 1994), Unit-1 is covering the top of a slump deposit, which is ~8 m thick. Therefore, it can be estimated that the age of the bottom of Unit 1 is ~29 kyr, which is consistent with the estimate in another region.

Isolated and relatively prominent acoustic blanking zones were observed below the S-ridge (Fig. 5a) and along the northeastern extension of the crest, below small hills, overlapped with high-strength backscatter, as inferred from the shipboard acoustic observations [Fig. 5c, (ii)]. The acoustic blanking zones did not penetrate Unit 1. The SBP section crossing the prominent bathymetric feature at the northern end of the knoll, a mound, and a depression, showed another acoustic blanking zone (see Fig. 2b, d).

Shallow faults and acoustic blanking zones recognized on the shipboard SBP sections were dense in the summit area, as observed by AUV, and rapidly became sparse away from the summit area (Fig. 2b). Discontinuities below a series of

anticlines corresponding to low ridges and shallow valleys in the southern part of the NW-slope were also observed in the shipboard SBP sections, similar to the AUV SBP sections (Fig. 5d). A large discontinuity of units was identified at the southeastern foot of the knoll, part of the reverse fault [Fig. 5e, (iii)], consistent with the AUV observations.

Discussion

Distribution of acoustically characteristic materials and bacterial mats on and below shallow seafloor

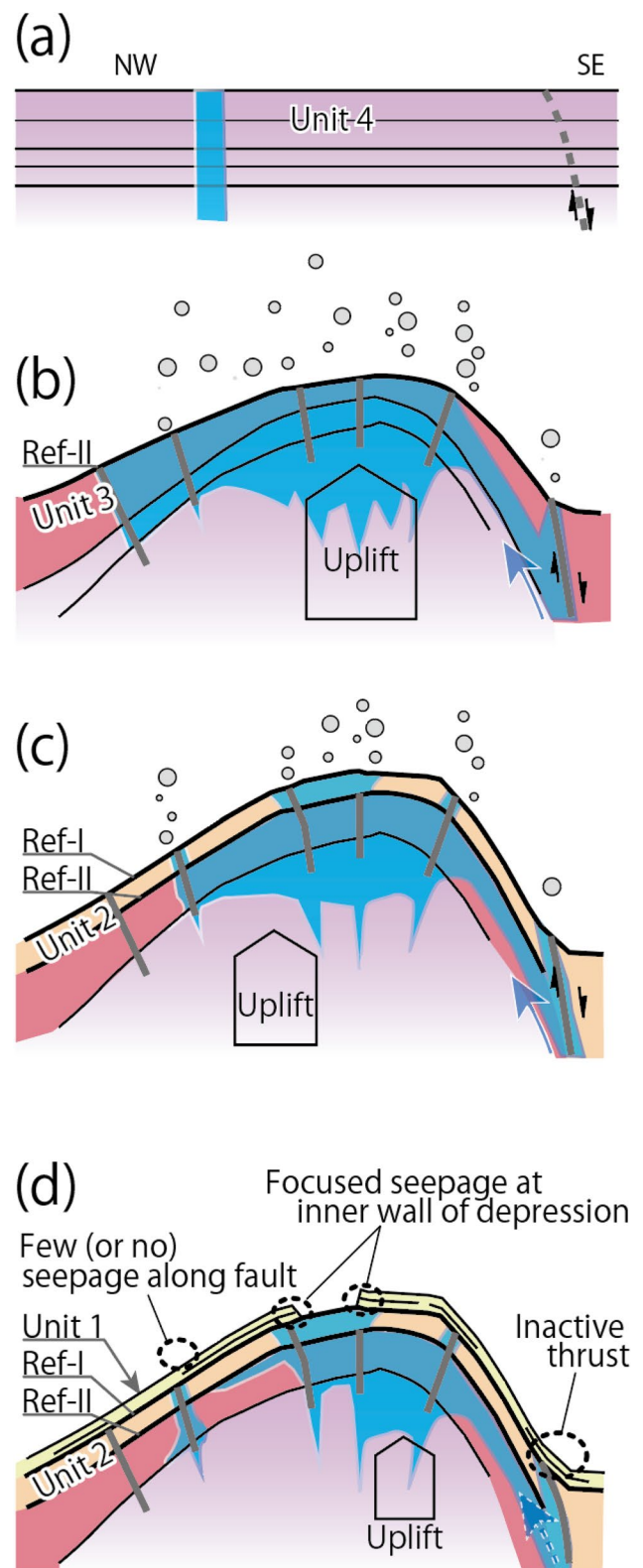
Outcrops on the GH-bearing seafloor were also observed off Joetsu, the other area harboring GHs ~200 km southwest of our target area (Matsumoto et al. 2009; Numanami and Matsumoto 2009) (see Fig. 1). The area off Joetsu is where the large amount of shallow GH has been confirmed (e.g., Matsumoto et al. 2009; Hiruta et al. 2009; Freire et al. 2011). Matsumoto et al. (2009) and Numanami and Matsumoto (2009) reported that the outcrops in the area off Joetsu are methane-derived authigenic carbonates (MDACs; Hovland et al. 1987; Aloisi et al. 2002; Buckman et al. 2020). Because of the similarity in tectonic setting and occurrence of the outcrops between the area off Joetsu and our target area, we consider that the outcrops

Fig. 8 Conceptual model illustrating geological features and formation processes of depression at the summit area of the knoll. Colors of Units are coinciding with Fig. 4. Black line: sediment layer. Gray bold line: shallow fault. Blue colored area: image of area filled by gas-bearing fluid from depth. **a** A period of deposition of Unit 4. Dotted line suggests an ancient fault, which will reactivate during following tectonic inversion. **b** A period of deposition of Unit 3. Large uplift that forms along the crest and roughly forms the current knoll. Acoustic blanking zone has widely formed. GHs possibly grew in this period. Slumping event has occurred with the uplifting of the knoll. **c** A period of deposition of Unit 2. Uplift has decreased but is continuous, and it has moved southwestward. Acoustic blanking has grown toward the seafloor at the central part. **d** Current status. GHs have formed until this stage at the top part of the anticline and dissociated, and then, depression was formed. Decreased gas emitted in a limited area along the intersection of permeable layers and scarps forming the depression. Gas appears to move along faults, but little or no gas is released through the present seafloor

are probably MDACs. MDACs are formed within shallow sediments and sulfate-methane transition zones by the mixing of methane and sulfate from seawater induced by sulfate-reducing bacteria and methane-utilizing archaea (Buckman et al. 2020).

As the outcrops have higher density and velocity than the surrounding unconsolidated clay-dominated sediments, the acoustic impedance contrast is greater between seawater and outcrops than between seawater and unconsolidated sediments. Similarly, shallow GHs, shelled animals, and sediments saturated by the gas-bearing fluid are potentially represented by the high-backscattering areas because their acoustic impedance contrasted with that of the surrounding unconsolidated clay-dominant sediments. The pattern of backscatter strength distribution between AUV and shipboard observations seems different, which is possibly attributable to different penetrations of acoustic signals due to different frequencies. Observations using AUVs (with higher frequency waves) reflect only the information on the seafloor, and observations using shipboard instruments (with lower frequency waves) reflect information on the part slightly below the seafloor. In other words, shipboard acoustic observations have the potential to visualize the distribution of materials that contrast greatly in acoustic impedance with the seafloor, not only when they are on the seafloor but also when they are below the seafloor.

MDACs are relatively stable on the seafloor and subsurface environments, they remain once they are produced (Watanabe et al. 2008; Crémière et al. 2016). Therefore, the presence of MDACs suggests that there was methane seepage. Contrary to the MDACs, bacterial mats are indicative of current seeps (Sahling et al., 2002; Boetius and Wenzhöfer, 2013). The limited distribution of bacterial mats rather than outcrops suggests that gas flux is presently limited. The fact that we observed neither a shallow GH nor bubbles on the present seafloor support this notion.



Inference of the uplifting periods of the Sakata Knoll

The characteristics of Units 1–4 reveal the formation history of the summit area of the Sakata Knoll for periods up to a depth of ~50 m. The change in thickness of each unit reveals the uplifting event. Figure 8 shows the conceptual model illustrating the process of knoll formation.

Thicknesses of Units 1, 2, and 3, values for the first and third quartiles excluding outliers, are 1.46–3.67 m, 7.34–16.25 m, and 12.52–23.75 m, respectively. The medians of Units 1, 2, and 3, in this case, are 2.52 m, 10.19 m, and 17.24 m, respectively. Unit 3 displays the largest thickness and variation.

Unit 1 tends to be thin at the SE side of the depression (Fig. 7). On the contrary, Unit 2 tends to be thin at the top of the SW side of the depression. Unit 3, the unit with the most variable thickness, tends to be thin along (or relatively southern part of) the crest line. After a relatively inactive period during the formation of Unit 4 (Fig. 8a), the period of the formation Unit 3 is considered to correspond to the timing when the topography of the knoll was roughly completed across the axis (Fig. 8b), followed by a gradual uplift on the SW side (Unit 2, Fig. 8c) and then on the SE side of the crest (Unit 1, Fig. 8d).

Transparent subunits found in Unit 3 are interpreted as a buried slumping event (e.g., Strasser et al. 2010; Moore et al. 2015), supporting the idea of an uplifting event that induces the movement of surface sediment during the formation of Unit 3. Fine sublayers found inside Unit 3b indicate that hemipelagic sedimentation continued with uplift during this period. Thicknesses of Units 1–3 tend to vary less and are stable in the northern part of the knoll (Fig. 7), indicating that the center of the uplift occurred in the southern part of the knoll during this period. The negative bathymetric features, which tend to be common on the southern part of the knoll, might be related to minor slide scars due to the deformation caused by the uplift. The unconformity at the lower limit of Unit 3 and the deformed but relatively constant thickness through Unit 4 indicate that the uplift was inactive in the period of Unit 4, at least in the area around the summit area of the knoll. Details regarding the age of each unit remain vague due to the limited dating information; however, some inferences can be made. Since Unit 2 appears at the bottom of the depression, which was formed after Reflector-I formation, sometime after 29–32 kyr, the formation age might coincide with the last glacial period (~22 kyr).

Acoustic blanking zone, its relationship with units, shallow faults, and current bathymetry

The acoustic blanking zone masks seafloor structures on SBP sections. Similar features have been reported in previous studies, such as acoustically transparent columnar disturbances, acoustic masking, acoustic turbidity, and acoustic voids (Judd and Hovland 2007). Judd and Hovland (2007) explained these features as being related to gas migration and gas escape structures through sediments. Matsumoto (2009) referred to a similar feature as a “gas chimney,” claiming it functioned as a gas movement path. In general, acoustic signals are scattered and reflected at the boundaries of physical properties. In addition, acoustic signals are attenuated along the propagation path. When propagating through the sediments filled by gas-bearing fluid, the attenuation is more significant compared to that through the normal water filled sediments (Dvorkin et al. 2014). Domenico (1976) suggested that fluids containing a small percentage of gas can dramatically reduce velocity and attenuate the amplitude of the acoustic signal. Priest et al. (2006) have reported that the attenuation of acoustic waves is sensitive to a small percentage of GH saturation. Although the acoustic blanking zone shown in our SBP should be a good indicator of the presence of gas-bearing fluid, it is difficult to quantify gas contents; hence, the acoustic blanking zone does not necessarily indicate the presence of a large amount of gas in the region.

Acoustic blanking zones on the northern part of the NW-slope mostly stop at the top of Unit 2, Reflector-I. The outstanding broad acoustic blanking zone below the depression and swells has two levels of top depth, it once stopped at the top of Unit 3a, Reflector-II, but then its center part broke through the Reflector-II, reaching Reflector-I (Figs. 3d and 8c). The rest of the acoustic blanking zones at the southern part of the knoll along the crest mostly stop at Reflector-II, and none of the acoustic blanking zones penetrated Unit 1. The acoustic blanking zone is widely distributed through Units 3 and 4. As a result, a part of the gas-bearing fluid formed GH in the summit area of the knoll.

Reflectors shown in SBP sections are interfaces between two layers with different acoustic impedance. In our target area, volcanic ash layers and/or gas-bearing layers are expected to be recognized as high-amplitude reflectors because they display a significant acoustic impedance contrast with the surrounding clay-dominant sediments. In the SBP sections, prominent high-amplitude reflectors appear to have good horizontal continuity. However, a closer observation reveals that these high-amplitude reflections do not necessarily occur between two specific layers. The positions where the high-amplitude reflections are generated often shift vertically to the boundary of the adjacent layer. Therefore, we interpret that such characteristic high-amplitude

reflectors with upward shifts do not indicate boundaries between specific geological formations but rather the top of gas-bearing layers with extremely low acoustic impedance.

High-amplitude reflectors are prominent on the SE-slope and are continuous with the reverse fault at the foot of the knoll. The reflectors connect the reverse fault at the southeastern foot to the summit area, fading toward the NW-slope. Therefore, the reflectors are considered routes to transport fluid from the reverse fault to the summit area of the knoll, while the gas-bearing fluid flows into the acoustic blanking zone and spots where the permeable layer is cut off. On the other hand, acoustic blanking does not deliver enough gas to the seafloor because none of the acoustic blanking zones penetrates Unit 1 and the limited distribution of bacterial mats, which are not necessarily distributed just above the acoustic blanking zones. Shallow faults recognized in SBP sections, which are mostly normal faults, do not always accompany acoustic blanking zones (Fig. 4), suggesting that they also do not necessarily play a major role as a route for fluid flow toward the seafloor. In the case of the Sakata Knoll, as far as ~50 m below the seafloor, the primary route of fluid flow consists of a reverse fault at the southeastern foot of the knoll and high-amplitude reflectors over the knoll, rather than acoustic blanking zones (Fig. 8). However, some shallow faults reaching the seafloor may exceptionally allow the fluid to pass to the seafloor and feed spotty bacterial mats, for instance, on top of swells.

Formation of depression and current distribution of shallow methane hydrate in the Sakata Knoll

Matsumoto (2009) suggested that the shallow GH had possibly dissociated due to the reduced pressure of seawater when the sea level dropped during the last glacial maximum. One of some possible causes of the dissociation of shallow buoyant GHs was because of a large shock over the area. As the bulk density of GHs is usually lower than that of seawater (e.g., Kieft et al. 1985; Pellenbarg and Max 2000), it is considered unstable if GHs and added gas are disturbed by events such as large earthquakes. Drain back may be another possibility for forming such a depression in the case of degassing from mud volcanoes and/or magmatic volcanoes (e.g., Sparks 2003). However, the Sakata Knoll originated from a tectonic inversion, and hence, it does not have a conduit, therefore drain back cannot be applied. In fact, horizontally continuous sedimentary layers were imaged beneath the depression in the seismic profiles (Yokota et al. 2022). For these reasons, we believe that the depression was formed by a buoyant collapse rather than a usual mass movement type collapse of the sediments (Fig. 8d). Our hypothesis is supported by the lack of disturbance of Unit 1, whereas the depression cuts Unit 1.

Terraces at both ends of the depression are considered to have remained during this event. The depths of both terraces are similar, and they are also close to the depth at which linear outcrops and bacterial mats were observed along the SE-slope side of the inner slope of the depression. The level may function to exclude dissociation at both ends of the depression when it was formed. The relatively complex shape and appearance of outcrops and bacterial mats on the northern terrace (indicating continuous seepage there) may be related to a relatively active northern side of the knoll, which is indicated by dominant positive bathymetric features on this side. Spotty distributed seepages can be seen where the seafloor locally dissociated on these swells. Our ROV observations found bacterial mats, indicators of current seepage (Sahling et al. 2002; Boetius and Wenzhöfer 2013), showing that limited distribution at the layer has been cut off and the occurrence of localized collapses. The isolated hill, small ridges, inner slope within the depression, and northern terrace within the depression may be influenced by the decreased, yet continuous, seepage through the permeable layers after the formation of the depression (Fig. 8d).

Tanahashi et al. (2017) reported LWD1407 (M05L) measurements obtained in the summit area of the knoll and the presence of GHs. Miyajima et al. (2022) reported that sedimentary coring revealed massive GHs from the point subject to LWD1406 (M04L) measurement at depths of 8–21 m below the seafloor. Although we did not directly observe GHs on the seafloor through ROV observation, we suggest that GHs are distributed in the shallow subseafloor over the summit area of the knoll. Although acoustic mapping cannot distinguish MDACs, shallow GHs, and sediment saturated with gas-bearing fluid only based on acoustic signals, acoustic mapping suggests the wider distribution of acoustically characteristic materials on the seafloor and the shallow subseafloor. Furthermore, the decreasing seepage suggests that a supply of fluid is presently decreased, principally occurring through the reverse fault of the southeastern foot of the knoll, flowing through permeable layers over the knoll. Such tectonically deformed topographic features, an anticline as a storage of gas-bearing fluid connecting to deeply (tectonically) developed faults as a route of gas-bearing fluid from depth, would be widespread in the northeast part of the Sea of Japan. We consider that such topographic features over the area can be recognized as potential areas for shallow GHs.

Conclusions

Acoustic mapping is beneficial in understanding the surface distribution of acoustic characteristics and the subseafloor structures in areas with shallow GHs. In the case of the Sakata Knoll, a shallow GH was confirmed by sediment

coring and suggested by LWD measurements, even though acoustic and optical observations did not directly detect bubbles or GHs on the seafloor. Based on a comparison of backscatter strength distributions obtained with AUV-equipped side-scan sonar and shipboard MBES, acoustically characteristic materials, such as MDACs and/or GHs, may be widespread in the shallow subseafloor. ROV operation suggested a limited distribution of bacterial mats, which illustrates that gas seepage is currently limited.

Interpretation of SBP sections revealed stratified layers and shallow faults, high-amplitude reflectors, and acoustic blanking zones for a depth of ~ 50 m below the seafloor. The high-amplitude reflectors are considered the top of the gas-bearing layers, continuing over the knoll toward the tectonically formed reverse fault. Since shallow faults do not necessarily accompany acoustic blanking zones, they do not play an important role as a fluid migration route, at least on the current seafloor. Consequently, in the case of the Sakata Knoll, we considered the main route of the fluid movement to the summit of the knoll to be the gas-bearing layers through the reverse fault from the deep rather than the acoustic blanking zones.

Based on the tracking of potential gas-bearing layers and bathymetric features, the depressions at the top of the knoll could have formed by the sufficient accumulation of gas-bearing fluid and the loss of buoyant volume after the formation of Reflector-I (and possibly during the formation of Unit 1). The partial volume at the top of the knoll detached and moved upwards because of the buoyancy of partially dissociated GHs than because of the surrounding sediment, forming the depression in the summit area of the knoll. Taking into account the estimation error, it is possible that the time of formation of the depression would have been 29–32 kyr, which roughly coincides with the last glacial maximum (~ 22 kyr). After that, the supply of gas-bearing fluid through layers likely decreased but remained continuous only in limited areas wherein the gas-bearing layer was cut off, such as at the inner scarp of the depression, isolated hill, small ridges, and over the northern terrace. A few seepage spots are observed also on the swells. Even if there is a decreased seepage of gas-bearing fluid at the summit area of the knoll, there are widely distributed GHs in the shallow subseafloor. Such GH-populated areas are considered widely distributed in the tectonically formed topographic features along the northeast part of the Sea of Japan.

Acknowledgements We appreciate the constructive comments and essential suggestions provided by two anonymous reviewers and the editor. We deeply thank Dr. Yusuke Miyajima and Dr. Hideyoshi Yoshioka for their helpful description of the outcrop and providing us with the photograph shown in Fig. 6c. We thank Kawasaki Geological Engineering Co., Ltd., Japan for carefully processing bathymetry data obtained by AUV Deep1. We also thank Mr. T. Koike (Kaiyo

Engineering Co., Ltd., Japan) for the output of the colored image obtained using ROV Kaiyo3000 and SeaXerocks1 after detailed processing such as the collection of attitudes and positioning and filtering. This study was conducted as a part of the methane hydrate research project funded by the Ministry of Economy, Trade, and Industry (METI), Japan. The Generic Mapping Tools software was used to generate bathymetric maps (Wessel & Smith 1998).

Author contributions Conceptualization: MA, MS; Methodology: MA, MS. Formal analysis and investigation: MA, MS, MT. Writing—original draft preparation: MA, TY. Writing—review and editing: MA, TY, MT, SG. Funding acquisition: MS, SG. Resources: MS, MT, SG. Supervision: TY, MT.

Funding This study was conducted as a part of a national project of gas hydrate research in the Sea of Japan funded by the Ministry of Economy, Trade and Industry (METI), Japan.

Data availability Because this study was conducted as a part of a national project of gas hydrate research in the Sea of Japan, we do not have permission to share data obtained in this project.

Declarations

Conflict of interest The authors declare that they have no known competing financial interest or personal relationships that could have appeared to influence the work reported in this paper.

Open Access This article is licensed under a Creative Commons Attribution 4.0 International License, which permits use, sharing, adaptation, distribution and reproduction in any medium or format, as long as you give appropriate credit to the original author(s) and the source, provide a link to the Creative Commons licence, and indicate if changes were made. The images or other third party material in this article are included in the article's Creative Commons licence, unless indicated otherwise in a credit line to the material. If material is not included in the article's Creative Commons licence and your intended use is not permitted by statutory regulation or exceeds the permitted use, you will need to obtain permission directly from the copyright holder. To view a copy of this licence, visit <http://creativecommons.org/licenses/by/4.0/>.

References

- Aloisi G, Bouloubassi I, Heijs SK, Pancost RD, Pierre C, Sinninghe Damste JS, Gottschal JC, Forney LJ, Rouchy J-M (2002) CH₄-consuming microorganisms and the formation of carbonate crusts at cold seeps. *Earth Planet Sci Lett* 203:195–203. [https://doi.org/10.1016/S0012-821X\(02\)00878-6](https://doi.org/10.1016/S0012-821X(02)00878-6)
- Bains S, Coefield RM, Norris RD (1999) Mechanism of climate warming at the end of the Paleocene. *Science* 285:724–727. <https://doi.org/10.1126/science.285.5428.724>
- Bodenmann A, Thornton B, Ura T (2016) Generation of high-resolution three-dimensional reconstructions of the seafloor in color using a single camera and structured light. *J Field Robotics* 34:833–851. <https://doi.org/10.1002/rob.21682>
- Boetius A, Wenzhöfer F (2013) Seafloor oxygen consumption fuelled by methane from cold seeps. *Nat Geosci* 6:725–734. <https://doi.org/10.1038/NGEO1926>
- Buckman J, Donnery T, Jiang Z, Lewis H, Ruffell A (2020) Methane derived authigenic carbonate (MDAC) aragonite cemented quaternary hardground from a methane cold seep, rathlin basin,

- Northern Ireland: $\delta^{13}\text{C}$ and $\delta^{18}\text{O}$ isotopes, environment, porosity and permeability. *Geosci* 10:255. <https://doi.org/10.3390/geosciences10070255>
- Crémière A, Lepland A, Chand S, Sahy D, Condon DJ, Noble SR, Martma T, Thorsnes T, Sauer S, Brunstad H (2016) Timescales of methane seepage on the Norwegian margin following collapse of the Scandinavian Ice Sheet. *Nat Commun* 7:11509. <https://doi.org/10.1038/ncomms11509>
- Dickens GR, O'Neil JR, Rea DK, Owen RM (1995) Dissociation of oceanic methane hydrate as a cause of the carbon-isotope excursion at the end of the Paleocene. *Paleoceanography* 10:965–971. <https://doi.org/10.1029/95PA02087>
- Domenico SN (1976) Effect of brine-gas mixture on velocity in an unconsolidated sand reservoir. *Geophys* 41:882–894. <https://doi.org/10.1190/1.1440670>
- Dvorkin J, Gutierrez M, Grana D (2014) Seismic wave attenuation. Seismic reflections of rock properties. Cambridge University Press, Cambridge, pp 239–261. <https://doi.org/10.1017/CBO9780511843655.021>
- Expedition 311 Scientists (2006) Expedition 311 summary. In: Riedel M, Collett TS, Malone MJ, and the Expedition 311 Scientists (ed), *Proc. IODP, 311*, Washington, DC (Integrated Ocean Drilling Program Management International, Inc.). <https://doi.org/10.2204/iodp.proc.311.101.2006>
- Freire AFM, Matsumoto R, Santos LA (2011) Structural-stratigraphic control on the Umitaka Spur gas hydrate of Joetsu Basin in the eastern margin of Japan Sea. *Mar Pet Geol* 28:1967–1978. <https://doi.org/10.1016/j.marpetgeo.2010.10.004>
- Ginsburg GD (1998) Gas hydrate accumulation in deep-water marine sediments. In: Heneriet JP, Mienert J (eds) *Gas hydrates: relevance to world margin stability and climate change*, vol 137. Geological Society, London, pp 51–62
- Hiruta A, Snyder GT, Tomaru H, Matsumoto R (2009) Geochemical constraints for the formation and dissociation of gas hydrate in an area of high methane flux, eastern margin of the Japan Sea. *Earth Planet Sci Lett* 279:326–339. <https://doi.org/10.1016/j.epsl.2009.01.015>
- Hovland M, Talbot MR, Qvale H, Olaussen S, Aasberg L (1987) Methane-related carbonate cements in pockmarks of the North Sea. *J Sed Petrol* 57:881–892. <https://doi.org/10.1306/212F8C92-2B24-11D7-8648000102C1865D>
- Ikehara M, Katayama H, Nakajima T (1994) Explanatory notes of sedimentological map of the vicinity of Awashima, *Marine Geology Map Series* 42, Geol Survey Japan.
- Judd A, Hovland M (2007) Pockmarks, shallow gas, and seeps: an initial appraisal. In: Judd A, Hovland M (eds) *Seabed fluid flow: the impact on geology, biology and the marine environment*. Cambridge University Press, Cambridge, pp 7–44. <https://doi.org/10.1017/CBO978051153918>
- Kieft H, Clouter MJ, Gagnon RE (1985) Determination of acoustic velocities of clathrate hydrates by Brillouin spectroscopy. *J Phys Chem* 89:3103–3108. <https://doi.org/10.1021/j100260a031>
- Kisimoto K (2000) Combined bathymetric and topographic mesh data: Japan250m.grd, in GSJ Open-file Report, NO.353, Geological Survey of Japan, Tsukuba, 2000.
- Kvenvolden KA (1988) Methane hydrate—A major reservoir of carbon in the shallow geosphere? *Chem Geol* 71:41–51. [https://doi.org/10.1016/0009-2541\(88\)90104-0](https://doi.org/10.1016/0009-2541(88)90104-0)
- Matsumoto R (1995) Causes of the $\delta^{13}\text{C}$ anomalies of carbonates and a new paradigm 'Gas-Hydrate Hypothesis.' *J Geol Soc Japan* 11:902–924. <https://doi.org/10.5575/geosoc.101.902>
- Matsumoto R (2009) Overview of gas hydrate: Impact of the discovery of a large ice-like carbon reservoir under the seafloor. *J Geograph* 118:7–42. [https://doi.org/10.5026/jgeography.118.7\(inJapaneseWithEnglishabstract\)](https://doi.org/10.5026/jgeography.118.7(inJapaneseWithEnglishabstract))
- Matsumoto R, Okuda Y, Hiruta A, Tomaru H, Takeuchi E, Sanno R, Suzuki M, Tsuchinaga K, Ishida Y, Ishizaki O, Takeuchi R, Komatsubara J, Freire AF, Machiyama H, Aoyama C, Joshima M, Hiromatsu M, Snyder G, Numanami H, Satoh M, Matoba Y, Nakagawa K, Kakuwa Y, Ogihara S, Yanagawa K, Sunamura M, Goto T, Lu H, Kobayashi T (2009) Formation and collapse of gas hydrate deposits in high methane flux area of the Joetsu Basin, eastern margin of Japan Sea. *J Geograph* 118:43–71. <https://doi.org/10.5026/jgeography.118.43>
- Matsumoto R, Ryu B-J, Lee S-R, Lin S, Wu S, Sain K, Pecher I, Riedel M (2011) Occurrence and exploration of gas hydrate in the marginal seas and continental margin of the Asia and Oceania region. *Mar Petrol Geol* 28:1751–1767. <https://doi.org/10.1016/j.marpetgeo.2011.09.009>
- Miyajima Y, Ota Y, Aoki S, Kaneko M, Yoshioka H, Takahashi HA, Ikawa R, Machida I, Tanahashi M, Suzuki K, Satoh M (2022) Geochemical characteristics of shallow gas hydrates and sediment pore waters obtained from 2021 drilling survey at Sakata Knoll, northeastern Japan Sea. *Japan Geosci. Union. Meet 2022. Abstr., MIS24-P01*, 2022. May. (Online and Chiba, Japan)
- Moore GF, Boston BB, Strasser M, Underwood MB, Ratliff RA (2015) Evolution of tectono-sedimentary systems in the Kumano Basin, Nankai Trough forearc. *Mar Petrol Geol* 67:604–616. <https://doi.org/10.1016/j.marpetgeo.2015.05.032>
- Nakajima T (2018) Tectonics of sedimentary basins in and around Japan since the opening of the Sea of Japan. *J Geol Soc Japan* 124:693–722. <https://doi.org/10.5575/geosoc.2018.0049> (in Japanese with English abstract)
- Nakajima T, Kikkawa K, Ikehara K, Katayama H, Kikawa E, Joshima M, Seto K (1996) Marine sediments and late Quaternary stratigraphy in the southeastern part of the Japan Sea—Concerning the timing of dark layer deposition. *J Geol Soc Japan* 102:125–138. <https://doi.org/10.5575/GEOSOC.102.125> (in Japanese with English abstract)
- Numanami H, Matsumoto R (2009) Pictorial 3: Seafloor environment and benthos of methane seep area. *J Geograph* 118:iii (in Japanese with English figure captions)
- Okamura Y, Watanabe M, Morijiri R, Sato M (1995) Rifting and basin inversion in the eastern margin of the Japan Sea. *Isl Arc* 4:66–181. <https://doi.org/10.1111/j.1440-1738.1995.tb00141.x>
- Okamura Y, Morijiri R, Sato M (1996) Explanatory notes of geological map West of Akita, *Marine Geology Map Series*, 48, Geol Survey Japan
- Otofuji Y, Hayashida A, Trii M (1985) When was the Japan Sea opened? Paleomagnetic evidence from Southwest Japan. In: Nasu N, Uyeda S, Kobayashi K, Kushiro I, Kagami H (eds) *Formation of active ocean margins*. Terrapub, Pozzuoli, pp 551–566
- Pellenbarg RE, Max MD (2000) Introduction, physical properties, and natural occurrences of hydrate. In: Max MD (ed) *Natural gas hydrate in oceanic and permafrost environments*. Springer, New York, pp 1–8
- Priest JA, Best AI, Clayton CRI (2006) Attenuation of seismic waves in methane gas hydrate-bearing sand. *Geophys J Int* 164:149–159. <https://doi.org/10.1111/j.1365-246X.2005.02831.x>
- Ruppel CD, Kessler JD (2017) The interaction of climate change and methane hydrates. *Rev Geophys* 55:126–168. <https://doi.org/10.1002/2016RG000534>
- Sahling H, Rickert D, Lee RW, Linke P, Suess E (2002) Macrofaunal community structure and sulfide flux at gas hydrate deposits from the Cascadia convergent margin, NE Pacific. *Mar Ecol Prog Ser* 231:121–138. <https://doi.org/10.3354/meps231121>
- Sloan ED Jr. (1998) Overview and historical perspective. *Clathrate hydrates of natural gases*. Marcel Dekker, Inc., New York

- Sparks RSJ (2003) Dynamics of magma degassing. In: Oppenheimer CP, Pyle DM, Barclay J (eds) Volcanic degassing, vol 213. Geological Society, London, pp 5–22
- Strasser M, Moore GF, Kimura G, Kopf AJ, Underwood MB, Guo J, Screamon EJ (2010) Slumping and mass transport deposition in the Nankai fore arc: evidence from IODP drilling and 3-D reflection seismic data. *Geochem Geophys Geosys* 12:5. <https://doi.org/10.1029/2010GC003431>
- Tamaki K (1988) Geological structure of the Japan Sea and its tectonic implications. *Bull Geol Survey Japan* 39:269–365
- Tanahashi M, Matsumoto R, Morita S (2017) Quantitative estimation of massive gas hydrate in gas chimney structures, the eastern margin of Japan Sea, from the physical property anomalies obtained by LWD, AGU fall meet. Abst., OS53C-2134, 2017. Dec. (New Orleans, USA).
- Watanabe Y, Nakai S, Hiruta A, Matsumoto R, Yoshida K (2008) U-Th dating of carbonate nodules from methane seeps off Joetsu, Eastern Margin of Japan Sea. *Earth Planet Sci Lett* 272:89–96. <https://doi.org/10.1016/j.epsl.2008.04.012>
- Watanabe M (1992) Preliminary report of the first occurrence horizon of *Pseudoeunotia doliolus* in sediment cores obtained from offshore of Yamagata and Akita prefectures (in Marine geological and geophysical studies around continental shelf along the eastern margin of central Japan Sea—Offshore of Yamagata and Akita prefectures-, Preliminary reports on researches in the 1991 Fiscal Year), Geological Survey of Japan, 203–205. (in Japanese)
- Yokota T, Yamaguchi K, Sato M, Goto S, Asada M, Teranishi Y, Higashinaka M (2022) High-resolution 3D seismic reflection survey of a shallow off Sakata, eastern margin of the Sea of Japan, Japan Geosci Union Meet 2022. abst, MIS26–04, 2022. May. (Online and Chiba, Japan).

Publisher's Note Springer Nature remains neutral with regard to jurisdictional claims in published maps and institutional affiliations.